PHYSICAL REVIEW B **89**, 064301 (2014)

Dynamical magnetic charges and linear magnetoelectricity

Meng Ye* and David Vanderbilt

Department of Physics and Astronomy, Rutgers University, Piscataway, New Jersey 08854-8019, USA

(Received 7 January 2014; revised manuscript received 17 January 2014; published 5 February 2014; publisher error corrected 21 February 2014)

Magnetoelectric (ME) materials are of fundamental interest and have been investigated for their broad potential for technological applications. The search for, and eventually the theoretical design of, materials with large ME couplings present challenging issues. First-principles methods have only recently been developed to calculate the full ME response tensor α including both electronic and ionic (i.e., lattice-mediated) contributions. The latter is proportional to both the Born dynamical electric charge Z^{e} and its analog, the dynamical magnetic charge Z^{m}. Here we present a theoretical study of the magnetic charge Z^{m} and the mechanisms that could enhance it. Using first-principles density functional methods, we calculate the atomic Z^{m} tensors in Cr_2O_3, a prototypical magnetoelectric, and in KITPite, a fictitious material that has previously been reported to show a strong ME response arising from exchange striction effects. Our results confirm that in Cr_2O_3, the Z^{m} values and resulting ME responses arise only from spin-orbit coupling (SOC) and are therefore rather weak. In KITPite, by contrast, the exchange striction acting on the noncollinear spin structure induces large Z^{m} values that persist even when SOC is completely absent.

DOI: 10.1103/PhysRevB.89.064301 PACS number(s): 75.85.+t, 75.30.Et, 71.15.Rf, 71.15.Mb

I. INTRODUCTION

There has been a recent resurgence of research on the magnetoelectric (ME) effect, which describes the coupling between electricity and magnetism [1]. The linear ME effect is defined as

$$\alpha_{\beta\nu} = \left.\frac{\partial P_\beta}{\partial H_\nu}\right|_{\mathcal{E}} = \mu_0 \left.\frac{\partial M_\nu}{\partial \mathcal{E}_\beta}\right|_{\mathbf{H}}, \tag{1}$$

where the polarization **P** is linearly induced by an external magnetic field **H**, or the magnetization is linearly generated by an applied electric field $\mathcal{E}$. Here indices β and ν denote the Cartesian directions and μ_0 is the vacuum permeability. This coupling between electricity and magnetism is of fundamental interest and shows broad potential for technological applications.

The history of research on the ME effect dates back to the 1960s when the magnetic symmetry started to be emphasized. It was first realized by Landau and Lifshitz that the ME response is only allowed in media without time-reversal symmetry or inversion symmetry [2]. In 1959, Dzyaloshinskii predicted that Cr_2O_3 should be a ME crystal [3] based on its magnetic point group, and experiments successfully measured the linear-induced magnetization by an external electric field [4,5] and the inverse effect [6]. The early theoretical studies and explanations for the ME effect were based on phenomenological models [7–10] that typically do not distinguish carefully between microscopic mechanisms. The recent rapid development of first-principles methods [11–13] has now allowed the underlying mechanisms in different materials to be classified and investigated.

The linear ME effect can be decoupled into three contributions, namely, electronic (frozen-ion), ionic (lattice-mediated), and strain-mediated responses [14]. Each term can be further subdivided into spin and orbital contributions. The early *ab initio* studies were focused on the spin-lattice [11] and spin-electronic [12] terms. First-principles methods have only recently been developed to calculate the full ME response tensor α, including both spin and orbital contributions [13]. As the symmetry condition for the strain-mediated term is more restrictive, this term is absent in most bulk materials.

Previous studies have shown that the spin-lattice term is dominant in many materials, as, for example, in Cr_2O_3 [13]. Íñiguez has shown [11] that the lattice contribution can be written as a product of the Born charge, the force-constant inverse, and the dynamical magnetic charge, which is the magnetic analog of the dynamical Born charge. This dynamical magnetic charge is defined as

$$Z^{\mathrm{m}}_{m\nu} = \Omega_0 \left.\frac{\partial M_\nu}{\partial u_m}\right|_{\mathcal{E},\mathbf{H},\eta}. \tag{2}$$

Here Ω_0 is the volume of the unit cell containing N atoms, and u_m denotes a periodicity-preserving sublattice displacement, where m is a composite label running from 1 to $3N$ to represent the atom and its displacement direction. The magnetic charge tensor Z^{m} plays an important role in various lattice-mediated magnetic responses and contributes to the Lyddane-Sachs-Teller relationship in magnetoelectric materials [15,16], but the mechanisms that give rise to it are not yet well understood. In particular, one route to optimizing the magnetoelectric coupling is clearly to enhance Z^{m}, but it is not obvious how to do so.

In this work, we use first-principles density functional methods to study the dynamical magnetic charges in two materials and explore the different mechanisms responsible for them in these two cases. We first study the magnetic charges in Cr_2O_3, which are driven by the spin-orbital coupling (SOC) mechanism. Then we study a fictitious structure, "KITPite," which was reported to have a large spin-lattice ME coupling according to a previous theory [17]. The structure of KITPite is such that the superexchange interactions between Mn moments are frustrated, leading to a 120° noncollinear spin structure. Our study shows that the Z^{m} values, which are orders of magnitude stronger than in Cr_2O_3, are responsible for the

*mengye@physics.rutgers.edu

strong ME coupling. We find that this enhancement is present even when SOC is completely absent, thus confirming that it arises from exchange striction acting on the noncollinear spins, in contrast to the case of Cr_2O_3 where $Z^{\rm m}$ is driven only by SOC effects.

The paper is organized as follows. In Sec. II A we introduce the formalism that describes how the dynamical magnetic charge tensor enters into the lattice contributions to the magnetic, ME, and piezomagnetic responses. In Sec. II B, we analyze the structure and the magnetic symmetry of Cr_2O_3 and KITPite. The computational details are described in Sec. II C. In Sec. III, we present and discuss the computed magnetic charge tensors for Cr_2O_3 and KITPite. Finally, Sec. IV provides a summary.

II. PRELIMINARIES

A. Formalism

Here, following Wojdel and Íñiguez [19], we generalize the formalism of Wu, Vanderbilt and Hamann [18] (WVH) to include the magnetic field, and use this systematic treatment to derive the ionic contribution of the ME coupling and other magnetic properties.

For an insulating system with N atoms in a unit cell, we consider four kinds of perturbation: (i) a homogeneous electric field $\boldsymbol{\mathcal{E}}$, whose indices β,γ run over $\{x,y,z\}$; (ii) a homogeneous magnetic field $\boldsymbol{H}$, whose indices ν,ω also run over $\{x,y,z\}$; (iii) a homogeneous strain $\boldsymbol{\eta}$, with Voigt indices $i,j=\{1\ldots6\}$; and (iv) internal displacements $\boldsymbol{u}$, indexed by composite labels m,n (atom and displacement direction) running over $1,\ldots,3N$. In this work we consider only internal displacements that preserve the bulk periodicity, corresponding to zone-center phonon modes.

The magnetoelectric enthalpy density is defined as

$$E(\boldsymbol{u},\boldsymbol{\eta},\boldsymbol{\mathcal{E}},\boldsymbol{H})=\frac{1}{\Omega_0}\left[E^{(0)}_{\rm cell}-\Omega(\mathcal{E}\cdot\mathbf{P}+\mu_0\mathbf{H}\cdot\mathbf{M})\right], \tag{3}$$

where $E^{(0)}_{\rm cell}$ is the the zero-field energy per cell, and Ω_0 and Ω are the undeformed and deformed cell volumes, respectively. $E(\boldsymbol{u},\boldsymbol{\eta},\boldsymbol{\mathcal{E}},\boldsymbol{H})$ can be expanded around the zero-field equilibrium structure as

$$\begin{aligned}E=\;&E_0+A_m u_m+A_j\eta_j+A_\beta\mathcal{E}_\beta+A_\nu H_\nu\\&+\tfrac{1}{2}B_{mn}u_m u_n+\tfrac{1}{2}B_{jk}\eta_j\eta_k+\tfrac{1}{2}B_{\beta\gamma}\mathcal{E}_\beta\mathcal{E}_\gamma\\&+\tfrac{1}{2}B_{\nu\omega}H_\nu H_\omega+B_{mj}u_m\eta_j+B_{m\beta}u_m\mathcal{E}_\beta\\&+B_{m\nu}u_m H_\nu+B_{\beta j}\mathcal{E}_\beta\eta_j+B_{\nu j}H_\nu\eta_j+B_{\beta\nu}\mathcal{E}_\beta H_\nu,\end{aligned} \tag{4}$$

where summation over repeated indices is implied. The coefficients of the first-order terms correspond to the atomic forces $F_m=-\Omega_0 A_m$, the stress tensor $\sigma_j=A_j$, the spontaneous polarization $P^{\rm S}_\beta=-A_\beta$, and the spontaneous magnetization $M^{\rm S}_\nu=-\mu_0^{-1}A_\nu$. For the equilibrium structure, the atomic forces and the stress tensor vanish. The diagonal second-order coefficients provide the force-constant matrix $K_{mn}=\Omega_0 B_{mn}$, the frozen-ion elastic tensor $\bar{C}_{jk}=B_{jk}$, the frozen-ion electric susceptibility $\bar{\chi}^{\rm e}_{\beta\gamma}=-\epsilon_0^{-1}B_{\beta\gamma}$, and the frozen-ion magnetic susceptibility $\bar{\chi}^{\rm m}_{\nu\omega}=-\mu_0^{-1}B_{\nu\omega}$, where the bar on a quantity indicates a purely electronic response computed at fixed internal coordinates of the atoms. The remaining terms correspond to off-diagonal responses, namely, the force-response internal-strain tensor $\Lambda_{mj}=-\Omega_0 B_{mj}$, the frozen-ion piezoelectric tensor $\bar{e}_{\beta j}=-B_{\beta j}$, the frozen-ion piezomagnetic tensor $\bar{h}_{\nu j}=-\mu_0^{-1}B_{\nu j}$, the frozen-ion magnetoelectric tensor $\bar{\alpha}_{\beta\nu}=-B_{\beta\nu}$, the atomic Born charges

$$Z^{\rm e}_{m\beta}=\Omega_0\frac{\partial P_\beta}{\partial u_m}\bigg|_{\mathcal{E},\mathbf{H},\eta}=\mu_0^{-1}\frac{\partial F_m}{\partial E_\beta}\bigg|_{\mathbf{H},\eta}=-\Omega_0 B_{m\beta}\,, \tag{5}$$

and the atomic magnetic charges

$$Z^{\rm m}_{m\nu}=\Omega_0\frac{\partial M_\nu}{\partial u_m}\bigg|_{\mathcal{E},\mathbf{H},\eta}=\mu_0^{-1}\frac{\partial F_m}{\partial H_\nu}\bigg|_{\mathcal{E},\eta}=-\Omega_0\mu_0^{-1}B_{m\nu}\,. \tag{6}$$

Static physical responses arise not only from the electronic part (barred quantities), but also from the ionic contribution associated with the change of the equilibrium internal displacements u_m with fields or strain. The relaxed-ion magnetoelectric enthalpy is

$$\tilde{E}(\boldsymbol{\eta},\boldsymbol{\mathcal{E}},\boldsymbol{H})=\min_{\boldsymbol{u}}E(\boldsymbol{u},\boldsymbol{\eta},\boldsymbol{\mathcal{E}},\boldsymbol{H})\,, \tag{7}$$

and the minimization is accomplished by substituting

$$u_m=-(B^{-1})_{mn}(B_{nj}\eta_j+B_{n\beta}\mathcal{E}_\beta+B_{n\nu}H_\nu) \tag{8}$$

into Eq. (4) to obtain the total relaxed-ion response (including both electronic and ionic parts). The total relaxed-ion electric susceptibility, magnetic susceptibility, and elastic, piezoelectric, piezomagnetic, and magnetoelectric tensors are then

$$\chi^{\rm e}_{\beta\gamma}=-\epsilon_0^{-1}\frac{\partial^2\tilde{E}}{\partial\mathcal{E}_\beta\partial\mathcal{E}_\gamma}\bigg|_{\mathbf{H},\eta}=\bar{\chi}^{\rm e}_{\beta\gamma}+\Omega_0^{-1}\epsilon_0^{-1}Z^{\rm e}_{m\beta}(K^{-1})_{mn}Z^{\rm e}_{n\gamma}\,, \tag{9}$$

$$\chi^{\rm m}_{\nu\omega}=-\mu_0^{-1}\frac{\partial^2\tilde{E}}{\partial H_\nu\partial H_\omega}\bigg|_{\mathcal{E},\eta}=\bar{\chi}^{\rm m}_{\nu\omega}+\Omega_0^{-1}\mu_0 Z^{\rm m}_{m\nu}(K^{-1})_{mn}Z^{\rm m}_{n\omega}\,, \tag{10}$$

$$C_{jk}=\frac{\partial^2\tilde{E}}{\partial\eta_j\partial\eta_k}\bigg|_{\mathcal{E},\mathbf{H}}=\bar{C}_{jk}-\Omega_0^{-1}\Lambda_{mj}(K^{-1})_{mn}\Lambda_{nj}\,, \tag{11}$$

$$e_{\beta j}=-\frac{\partial^2\tilde{E}}{\partial\mathcal{E}_\beta\partial\eta_j}\bigg|_{\mathbf{H}}=\bar{e}_{\beta j}+\Omega_0^{-1}Z^{\rm e}_{m\beta}(K^{-1})_{mn}\Lambda_{nj}\,, \tag{12}$$

$$h_{\nu j}=-\frac{\partial^2\tilde{E}}{\partial H_\nu\partial\eta_j}\bigg|_{\mathcal{E}}=\bar{h}_{\nu j}+\Omega_0^{-1}Z^{\rm m}_{m\nu}(K^{-1})_{mn}\Lambda_{nj}\,, \tag{13}$$

$$\alpha_{\beta\nu}=-\frac{\partial^2\tilde{E}}{\partial\mathcal{E}_\beta\partial H_\nu}\bigg|_{\eta}=\bar{\alpha}_{\beta\nu}+\Omega_0^{-1}\mu_0 Z^{\rm e}_{m\beta}(K^{-1})_{mn}Z^{\rm m}_{n\nu}\,. \tag{14}$$

The six lattice-mediated responses in Eqs. (9)–(14) are all made up of four fundamental tensors: the Born charge tensor $Z^{\rm e}$, the magnetic charge tensor $Z^{\rm m}$, the internal strain tensor Λ, and the inverse force-constant matrix K^{-1}. The manner in which these six lattice responses are computed from the four fundamental tensors is illustrated in Fig. 1, which depicts the linear-response connections between elastic, electric, and magnetic degrees of freedom.

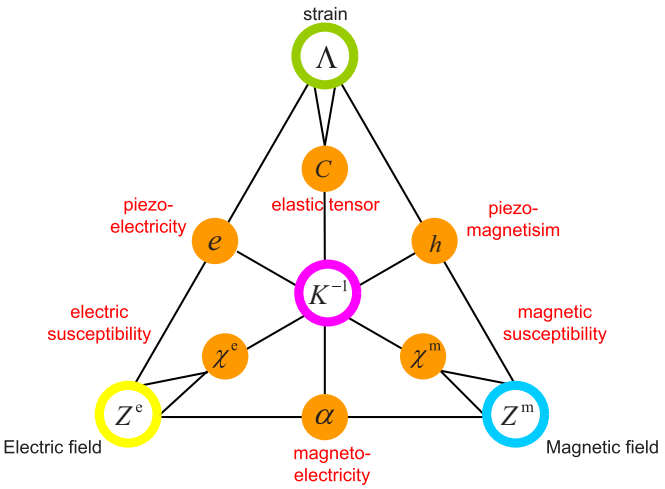

FIG. 1. (Color online) Sketch showing how the six lattice-mediated responses indicated by solid circles (orange) are each built up from the four elementary tensors indicated by open circles: the Born charge Z^{e} (yellow), magnetic charge Z^{m} (blue), internal strain Λ (green), and force-constant inverse K^{-1} (magenta). Each lattice-mediated response is given by the product of the three elementary tensors connected to it, as indicated explicitly in Eqs. (9)–(14).

If the crystal symmetry is low enough that piezoelectric or piezomagnetic effects are present, then the strain degrees of freedom can similarly be eliminated by minimizing the magnetoelectric enthalpy with respect to them, leading to additional strain-relaxation contributions to χ^{e}, χ^{m}, and/or α. We do not consider these contributions in the present work because such terms are absent by symmetry in the materials under consideration here.

The above derivations are carried out in the $(\mathcal{E},\mathbf{H})$ frame, which is consistent with the usual experimental conventions. In the context of first-principles calculations, however, it is more natural to work in the $(\mathcal{E},\mathbf{B})$ frame, as $\mathcal{E}$ and $\mathbf{B}$ are directly related to the scalar and vector potentials ϕ and $\mathbf{A}$. The magnetoelectric tensor α has different units in these two frames. In the $(\mathcal{E},\mathbf{H})$ frame, α is defined through Eq. (14) so that the units are s/m. In the $(\mathcal{E},\mathbf{B})$ frame, α is instead defined as

$$\alpha_{\beta\nu}^{\mathcal{E}\mathbf{B}} = \left.\frac{\partial M_\nu}{\partial \mathcal{E}_\beta}\right|_{\mathbf{B}} = \left.\frac{\partial P_\beta}{\partial B_\nu}\right|_{\mathcal{E}} \tag{15}$$

and carries units of inverse ohm, the same as for $\sqrt{\epsilon_0/\mu_0}$, the inverse of the impedance of free space. The ME tensors in these two frames are related by $\alpha^{\mathcal{E}\mathbf{H}} = (\mu\alpha)^{\mathcal{E}\mathbf{B}}$, where μ is the magnetic permeability. The electric and magnetic dynamical charges in the two frames are related by $(Z^{\mathrm{e}})^{\mathcal{E}\mathbf{H}} = (Z^{\mathrm{e}} + \alpha\mu Z^{\mathrm{m}})^{\mathcal{E}\mathbf{B}}$ and $(Z^{\mathrm{m}})^{\mathcal{E}\mathbf{H}} = (\mu Z^{\mathrm{m}}/\mu_0)^{\mathcal{E}\mathbf{B}}$.

For nonferromagnetic materials we have $\mu \approx \mu_0$, so that the Z^{m} values are essentially the same in the two frames. The same is also true for Z^{e}, since the product $(\alpha\mu Z^{\mathrm{m}})^{\mathcal{E}\mathbf{B}}$ is at least 5 orders of magnitude smaller than Z^{e} in most magnetoelectric materials. In this work we report our results in the more conventional $(\mathcal{E},\mathbf{H})$ frame, even though the computations are carried out in the $(\mathcal{E},\mathbf{B})$ frame.

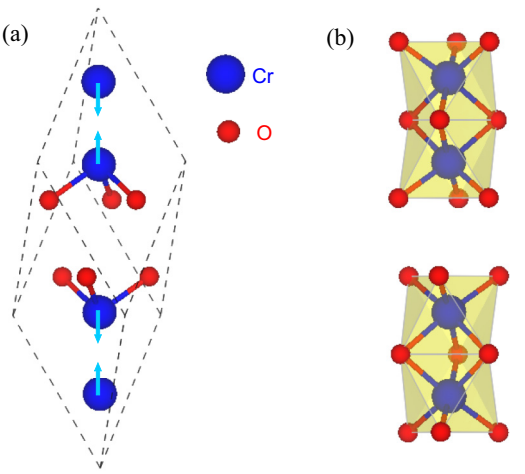

FIG. 2. (Color online) Structure of Cr_2O_3. (a) In the rhombohedral primitive cell, four Cr atoms align along the rhombohedral axis with AFM magnetic moments shown by (blue) arrows. (b) Each Cr atom is at the center of a distorted oxygen octahedron.

B. Structure and symmetry

1. Cr_2O_3

Cr_2O_3 adopts the corundum structure with two formula units per rhombohedral primitive cell, as shown in Fig. 2(a). Each Cr atom is at the center of a distorted oxygen octahedron as shown in Fig. 2(b). It is an antiferromagnetic (AFM) insulator up to the Néel temperature $T_{\mathrm{N}} = 307$ K. The AFM phase has the magnetic space group $R\bar{3}'c'$, and the spin direction on the Cr atoms alternates along the rhombohedral axis. The magnetic symmetry allows a nonzero ME tensor with two independent components $\alpha_\perp = \alpha_{xx} = \alpha_{yy}$ and $\alpha_\parallel = \alpha_{zz}$. Another feature of this magnetic group is that all the improper rotations are coupled to the time-reversal operator and vise versa, so that pseudovectors and ordinary vectors transform in the same way, implying that the magnetic charge Z^{m} and the Born charge Z^{e} have the same tensor forms. The threefold symmetry on each Cr atom restricts its tensor to have the form shown in Fig. 3(a). The symmetry is lower on the O atoms; for

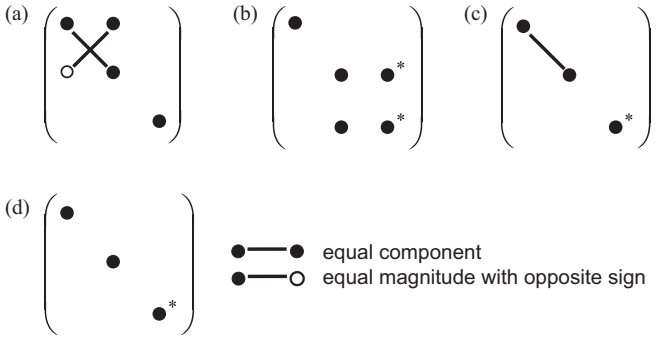

FIG. 3. Symmetry pattern of the Born and magnetic charge tensors for (a) the Cr atom in Cr_2O_3, (b) the O atom in Cr_2O_3, and the O^2 atom in $CaAlMn_3O_7$, (c) the Ca, Al, and O^1 atoms in $CaAlMn_3O_7$, and (d) the Mn and O^3 atoms in $CaAlMn_3O_7$. The elements indicated by an asterisk vanish in the absence of SOC for Z^{m} in $CaAlMn_3O_7$.

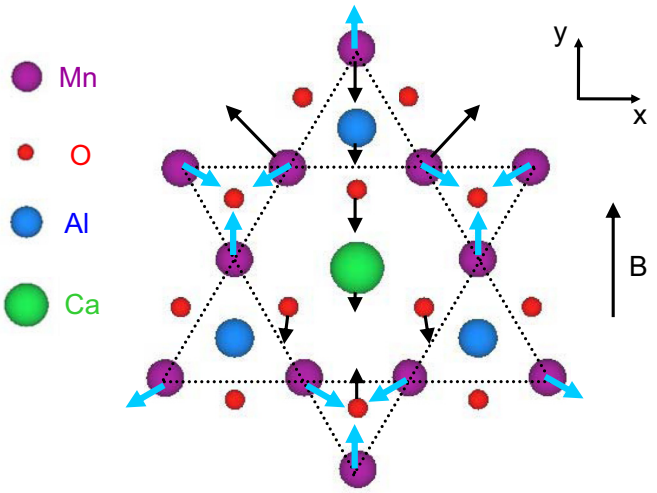

FIG. 4. (Color online) Planar view of the $CaAlMn_3O_7$ (KITPite) structure. The broad arrows (blue) on the Mn atoms represent the magnetic moment directions in the absence of electric or magnetic fields. Small (black) arrows indicate the atomic forces induced by an external magnetic field applied in the $\hat{y}$ direction.

the one lying on the twofold rotation axis along $\hat{x}$, for example, the charge tensor takes the form shown in Fig. 3(b).

2. KITPite

The fictitious "KITPite" structure with chemical formula $CaAlMn_3O_7$ is kagome-like with 120° in-plane AFM spin ordering, as shown in Fig. 4. The unit cell includes two formula units made by stacking two MnO layers with 180° rotations between layers. Each Mn atom is surrounded by an oxygen bipyramid and the O atoms are in three nonequivalent Wyckoff positions: O^1 are in the voids of the Mn triangles; O^2 are the apical ions located between the two MnO layers (not shown in the planar view); and O^3 form the MnO hexagons. The magnetic space group is $6_3/m'm'c'$; this has the same symmetry feature as Cr_2O_3, namely that all the improper rotations and time-reversal symmetries are coupled together, so that the Born charges and the magnetic charges follow the same symmetry restrictions. The charge tensors for Ca, Al, and O^1 atoms have the symmetry pattern shown in Fig. 3(c), and the Mn and O^3 atoms have the charge tensor form of Fig. 3(d). For the apical O^2 atoms, the five independent components in the charge tensor can be written in the form of Fig. 3(b) when the on-site twofold axis is along the $\hat{x}$ direction.

The elements marked by asterisks in Fig. 3 are those that vanish for Z^m in $CaAlMn_3O_7$ when SOC is neglected. The system of magnetic moments is exactly coplanar in the absence of SOC, and will remain so even after the application of any first-order nonmagnetic perturbation. Thus spin components along $\hat{z}$ cannot be induced, and it follows that the elements in the third column all vanish in all atomic Z^m tensors in $CaAlMn_3O_7$ when SOC is neglected.

C. First-principles methods

The first-principles calculations for Cr_2O_3 are performed with the QUANTUM ESPRESSO [20] package using the generalized-gradient approximation parametrized by the Perdew-Burke-Ernzerhof functional [21]. We employ Troullier-Martins norm-conserving pseudopotentials [22] with SOC included and Cr $3s$ and $3p$ states incorporated in the valence. The wave functions are expanded in a plane-wave basis with cutoff energy 150 Ry, and a $4 \times 4 \times 4$ Monkhorst-Pack k-point mesh is used for the self-consistent-field loop. In the Berry-phase polarization calculation [23], a $4 \times 4 \times 5$ k-point sampling is found to be sufficient. In order to calculate magnetic charges, Born effective charges, and the Γ-point force-constant matrix, the finite-difference method is used by displacing each atomic sublattice in each Cartesian direction and computing the total magnetization, the Berry-phase polarization, and the Hellmann-Feynman forces. The orbital magnetization is calculated using the modern theory of orbital magnetization [24–26].

The calculations for the fictitious KITPite material are carried out with plane-wave density functional theory implemented in VASP [27]. Projector augmented wave (PAW) pseudopotentials [28] with a 400-eV energy cutoff are sufficient in the noncollinear magnetization computation without SOC. For the exchange-correlation functional we use the rotationally invariant LSDA + U functional [29], with Hubbard $U = 5.5$ eV and $J = 2.0$ eV on the d orbitals of the Mn atoms [30]. The Born effective charge tensor and the Γ-point force-constant matrix are obtained by linear-response methods. The dynamical magnetic charges are computed by applying a uniform Zeeman field in the crystal and computing the resulting forces [12]. A $4 \times 4 \times 4$ Monkhorst-Pack k-point mesh is used in the calculations.

III. RESULTS

A. Cr_2O_3

The Cr_2O_3 ground-state structural parameters predicted by our first-principles calculations are in good agreement with experiment, as shown in Table I. A group-theory analysis of the long-wavelength phonons shows that the infrared (IR) active phonon modes, which couple to the electromagnetic excitations, are the longitudinally active A_{2u} modes and the transversely active doubly degenerated E_u modes,

$$\Gamma_{\mathrm{IR}} = 2A_{2u} + 4E_u\,, \tag{16}$$

where the acoustic modes have been excluded. The IR-active mode frequencies shown in Table II are computed using linear-response methods, and the results are in good agreement with experiment.

TABLE I. Structural parameters of Cr_2O_3 from first-principles calculation and experiments: rhombohedral lattice constant a, lattice angle α, and Wyckoff positions for Cr(4c) and O(6e).

			Wyckoff position	
	a (Å)	α (deg)	Cr	O
This work	5.386	54.3	0.1546	0.0617
Expt. (Ref. [33])	5.358	55.0	0.1528	0.0566

TABLE II. Frequencies (cm^{-1}) of zone-center IR-active phonon modes of Cr_2O_3 from first-principles calculations and experiments. The two A_{2u} modes are IR-active along z; the four E_u modes are IR-active in the x-y plane (doubly degenerate).

	A_{2u} modes		E_u modes			
This work	388	522	297	427	510	610
Expt. (Ref. [31])	402	533	305	440	538	609

The main results for the magnetic charge tensors of Cr_2O_3 are reported both in the atomic basis and in the IR-active mode basis in Tables III and IV. The spin contributions are dominant in the transverse direction but much weaker in the longitudinal direction. This is to be expected from the nearly collinear spin order of Cr_2O_3, considering that the magnitudes of the magnetic moments are quite stiff while their orientations are relatively free to rotate. The main effect in the longitudinal direction is from the orbital-magnetization contribution. Incidentally, we also find that the longitudinal components of the magnetic charge for Cr atoms are very sensitive to the lattice constant of Cr_2O_3, especially the Cr-O distance in the longitudinal direction. Thus it is essential to choose a proper exchange-correlation functional to mimic the experimental ground-state structure.

The Born charge tensors for Cr and O are computed to be

$$Z^{\mathrm{e}}(\mathrm{Cr}) = \begin{pmatrix} 3.02 & -0.30 & 0 \\ 0.30 & 3.02 & 0 \\ 0 & 0 & 3.18 \end{pmatrix} e\,,$$

$$Z^{\mathrm{e}}(\mathrm{O}) = \begin{pmatrix} -2.36 & 0 & 0 \\ 0 & -1.66 & -1.00 \\ 0 & -0.88 & -2.12 \end{pmatrix} e\,.$$

While the symmetry constraints on the nonzero elements are the same as for Z^{m}, the pattern is quite different. For example, the diagonal elements are of similar magnitude for Z^{e} but not for Z^{m}.

The lattice-mediated magnetic and electric responses for Cr_2O_3 computed from Eqs. (9)–(14) are summarized in the bottom panel of Table IV. Our computational results are in reasonable agreement with the experimental room-temperature lattice-mediated $\chi^{\mathrm{e}}_{\parallel} = 4.96$ and $\chi^{\mathrm{e}}_{\perp} = 3.60$ obtained from IR reflectance measurements [31]. In contrast, the experimentally measured longitudinal and transverse magnetic susceptibility at low temperature [32] are on the order of $\sim 10^{-3}$, which is about 5 orders of magnitude larger than the results obtained from Eq. (10). This difference undoubtedly arises from the fact that the experimental χ^{m} is dominated by the electronic (i.e., frozen-ion) contribution $\bar{\chi}^{\mathrm{m}}$ that is not included in Table IV. The magnetoelectric response $\alpha_{\parallel}$ and $\alpha_{\perp}$ both agree closely with previous theory, which is in reasonable agreement with experiment [11,13].

TABLE III. Magnetic charges Z^{m} ($10^{-2}\mu_{\mathrm{B}}/\text{Å}$) for Cr_2O_3 in the atomic basis. The magnetic charge tensors for Cr and O atoms take the forms shown in Figs. 3(a) and 3(b).

	Spin	Orbital		Spin	Orbital
Z^{m}_{xx}(Cr)	5.88	0.25	Z^{m}_{yy}(O)	−1.95	−0.38
Z^{m}_{xy}(Cr)	−5.69	0.02	Z^{m}_{yz}(O)	0.00	1.12
Z^{m}_{zz}(Cr)	0.02	0.23	Z^{m}_{zy}(O)	−1.10	−0.72
Z^{m}_{xx}(O)	−5.92	0.06	Z^{m}_{zz}(O)	−0.02	−0.15

TABLE IV. Top: Mode decomposition of the Born charges Z^{e}, and of the spin and orbital contributions to the magnetic charges Z^{m}, in Cr_2O_3. C_n are the eigenvalues of the force-constant matrix. Bottom: Total A_{2u}-mode (longitudinal) and E_u-mode (transverse) elements of the lattice-mediated electric susceptibility χ^{e}, magnetic susceptibility χ^{m}, and the spin and orbital pars of the ME constant α.

	A_{2u} modes		E_u modes			
C_n (eV/Å^2)	10.5	22.9	10.2	16.0	20.2	30.9
Z^{e} (|e|)	1.15	8.50	0.55	0.39	3.71	7.07
$Z^{\mathrm{m}}_{\mathrm{spin}}$ ($10^{-2}\mu_{\mathrm{B}}$/Å)	0.02	0.05	−0.76	−3.97	16.14	10.55
$Z^{\mathrm{m}}_{\mathrm{orb}}$ ($10^{-2}\mu_{\mathrm{B}}$/Å)	2.74	−0.59	0.66	−0.80	−0.29	1.06
Latt. χ^{e}	6.2		4.37			
Latt. χ^{m}	0.05×10^{-8}		1.28×10^{-8}			
α_{spin} (ps/m)	0.0024		0.633			
α_{orb} (ps/m)	0.0097		0.025			

B. KITPite

When we relax KITPite $CaAlMn_3O_7$ in the assumed $6_3/m'm'c'$ structure, the unit cell has a volume of 311.05 Å^3 with a c/a ratio of 0.998. The Wyckoff coordinates for the Mn atoms (6h) and O^3 atoms (6g) are 0.5216 and 0.1871. Other atoms are in high-symmetry Wyckoff positions. The IR-active modes are

$$\Gamma_{\mathrm{IR}} = 6A_{2u} + 9E_{1u}, \tag{17}$$

excluding the acoustic modes. The A_{2u} modes do not contribute to the magnetic response when spin-orbit interaction is absent in $CaAlMn_3O_7$, because the longitudinal components of the magnetic charges Z^{m} are zero.

The results for the magnetic charge tensors are reported in the atomic basis and the IR-active mode basis in Tables V and VI, respectively. The calculated force-constant eigenvalues and Born charges Z^{e} are also listed in Table VI. The Born charges in KITPite and Cr_2O_3 are all close to the atomic

TABLE V. Magnetic charges Z^{m} ($10^{-2}\mu_{\mathrm{B}}$/Å) for $CaAlMn_3O_7$ (KITPite) in the atomic basis (spin only). The magnetic charge tensors for Ca, Al, and O^1 are of the form of Fig. 3(c); those for Mn and O^3 are of the form of Fig. 3(d); and that for O^2 is of the form of Fig. 3(b).

	Z^{m} ($10^{-2}\mu_{\mathrm{B}}$/Å)		
Z^{m}_{xx}(Ca)	−43.46	Z^{m}_{xx}(O^2)	−39.15
Z^{m}_{xx}(Al)	−24.63	Z^{m}_{yy}(O^2)	1.23
Z^{m}_{xx}(Mn)	341.53	Z^{m}_{zy}(O^2)	−37.62
Z^{m}_{yy}(Mn)	−171.46	Z^{m}_{xx}(O^3)	−56.09
Z^{m}_{xx}(O^1)	66.98	Z^{m}_{yy}(O^3)	−75.23

TABLE VI. The Born charges Z^e and the magnetic charges Z^m for the IR-active A_{2u} modes in $CaAlMn_3O_7$. C_n are the eigenvalues of the force-constant matrix.

C_n (eV/Å^2)	Z^e (|e|)	Z^m_{spin} ($10^{-2}\mu_B$/Å)
–2.4	3.7	539.7
–1.1	4.7	17.2
2.8	4.3	−0.6
7.1	2.4	266.4
11.6	5.1	−107.8
12.0	2.4	−74.5
35.3	7.9	−15.9
46.7	2.2	34.8
55.1	4.6	−325.7

valence charge values. As the KITPite structure is fictitious and two E_{1u} modes are unstable in the high-symmetry structure, we will focus on the results for the magnetic charges and omit any discussion of the the magnetic and dielectric responses.

The magnetic charges in the KITPite structure are found to be much larger than for Cr_2O_3. For the transition-metal ion, the magnetic charge of Mn in KITPite is ∼50 times larger than for Cr in Cr_2O_3. The magnetic charges in Cr_2O_3 are driven by SOC, which acts as an antisymmetric exchange field. Thus the weakness of the SOC on the Cr atoms implies that the magnetic charges and magnetic responses are small in Cr_2O_3. In the KITPite structure, we deliberately exclude spin-orbit interaction, so the magnetic charges are purely induced by the spin frustration and the superexchange between Mn-O-Mn atoms. This exchange striction mechanism causes the magnetic charges in $CaAlMn_3O_7$ to be dozens of times larger than the SOC-driven responses in Cr_2O_3.

Since the orbital magnetization is strongly quenched in most 3*d* transition metals, we expect the orbital contribution to the Z^m tensors in $CaAlMn_3O_7$ to be comparable with those in Cr_2O_3, i.e., on the order of $10^{-2}\,\mu_B$/Å. Since this is ∼2 orders of magnitude smaller than the typical spin contribution in $CaAlMn_3O_7$, we have not included it in our calculation. The main point of our study of KITPite $CaAlMn_3O_7$ has been to demonstrate that exchange-striction effects can give rise to large Z^m values based on a mechanism that does not involve SOC at all.

IV. SUMMARY

In summary, we have begun by presenting a systematic formulation of the role played by the dynamic magnetic charge tensor Z^m in the lattice magnetic, magnetoelectric, and piezomagnetic responses of crystalline solids. We have then used first-principles density functional methods to compute the atomic Z^m tensors for two prototypical materials, namely, Cr_2O_3, a well-studied magnetoelectric material, and fictitious KITPite, which displays a very large lattice ME effect. We find that the physics is quite different in the two cases, with mechanisms based on SOC giving only small Z^m values in the collinear antiferromagnet Cr_2O_3, while exchange-striction effects induce very large Z^m values in noncollinear KITPite.

Our calculations are part of a broader effort to identify mechanisms that could induce large magnetic charge values. They help to reinforce a picture in which SOC effects give only weak contributions, at least in 3*d* transition-metal compounds, whereas exchange striction can induce much larger effects in materials in which spin frustration gives rise to a noncollinear spin structure. In this respect, the conclusions parallel those that have emerged with respect to the polarization in multiferroics and magnetically-induced improper ferroelectrics, where exchange striction, when present, typically produces much larger effects than SOC [34].

Our work points to some possible future directions for exploration. One obvious direction is to identify experimentally known materials in which exchange striction gives rise to large Z^m values. In such systems, lattice-mediated effects might even contribute significantly to the magnetic susceptibility; while such contributions are normally neglected for χ^m, we note that Z^m appears to the second power in Eq. (10), so this contribution might be significant, especially in soft-mode systems. It might also be interesting to explore the role of these magnetic charges in the phenomenology of electromagnons [35]. Finally, we point out that unlike Z^e, Z^m remains well defined even in metals; while magnetoelectric effects do not exist in this case, it would still be interesting to explore the consequences of large Z^m values in such systems.

ACKNOWLEDGMENT

This work was supported by the ONR, Grant No. N00014-12-1-1035.

[1] M. Fiebig, J. Phys. D **38**, R123 (2005).
[2] L. D. Landau and E. M. Lifshitz, *Electrodynamics of Continuous Media*, Course of Theoretical Physics, Vol. 8 (Pergamon Press, Oxford, 1960).
[3] I. E. Dzyaloshinskii, J. Exp. Theor. Phys. **37**, 881 (1959).
[4] D. N. Astrov, J. Exp. Theor. Phys. **38**, 984 (1960).
[5] V. J. Folen, G. T. Rado, and E. W. Stalder, Phys. Rev. Lett. **6**, 607 (1961).
[6] G. T. Rado and V. J. Folen, Phys. Rev. Lett. **7**, 310 (1961).
[7] G. T. Rado, Phys. Rev. Lett. **6**, 609 (1961).
[8] G. T. Rado, Phys. Rev. **128**, 2546 (1962).
[9] R. Hornreich and S. Shtrikman, Phys. Rev. **161**, 506 (1967).
[10] O. F. de Alcantara Bonfim and G. A. Gehring, Adv. Phys. **29**, 731 (1980).
[11] J. Íñiguez, Phys. Rev. Lett. **101**, 117201 (2008).
[12] E. Bousquet, N. A. Spaldin, and K. T. Delaney, Phys. Rev. Lett. **106**, 107202 (2011).
[13] A. Malashevich, S. Coh, I. Souza, and D. Vanderbilt, Phys. Rev. B **86**, 094430 (2012).
[14] T. Birol, N. A. Benedek, H. Das, A. L. Wysocki, A. T. Mulder, B. M. Abbett, E. H. Smith, S. Ghosh, and C. J. Fennie, Curr. Opin. Solid State Mater. Sci. **16**, 227 (2012).
[15] R. Resta, Phys. Rev. Lett. **106**, 047202 (2011).
[16] R. Resta, Phys. Rev. B **84**, 214428 (2011).
[17] K. T. Delaney, M. Mostovoy, and N. A. Spaldin, Phys. Rev. Lett **102**, 157203 (2009).
[18] X. Wu, D. Vanderbilt, and D. R. Hamann, Phys. Rev. B **72**, 035105 (2005).

[19] J. C. Wojdel and J. Íñiguez, Phys. Rev. Lett. **103**, 267205 (2009).
[20] P. Giannozzi, S. Baroni, N. Bonini, M. Calandra, R. Car, C. Cavazzoni, D. Ceresoli, G. L. Chiarotti, M. Cococcioni, I. Dabo *et al*., J. Phys.: Condens. Matter **21**, 395502 (2009).
[21] J. P. Perdew, K. Burke, and M. Ernzerhof, Phys. Rev. Lett. **77**, 3865 (1996).
[22] N. Troullier and J. L. Martins, Phys. Rev. B **43**, 1993 (1991).
[23] R. D. King-Smith and D. Vanderbilt, Phys. Rev. B **47**, 1651 (1993).
[24] D. Xiao, J. Shi, and Q. Niu, Phys. Rev. Lett. **95**, 137204 (2005).
[25] T. Thonhauser, D. Ceresoli, D. Vanderbilt, and R. Resta, Phys. Rev. Lett. **95**, 137205 (2005).
[26] D. Ceresoli, T. Thonhauser, D. Vanderbilt, and R. Resta, Phys. Rev. B **74**, 024408 (2006).
[27] G. Kresse and J. Furthmüller, Phys. Rev. B **54**, 11169 (1996).
[28] P. E. Blochl, Phys. Rev. B **50**, 17953 (1994); G. Kresse and D. Joubert, *ibid*. **59**, 1758 (1999).
[29] A. I. Liechtenstein, V. I. Anisimov, and J. Zaanen, Phys. Rev. B **52**, R5467 (1995).
[30] Z. Yang, Z. Huang, L. Ye, and X. Xie, Phys. Rev. B **60**, 15674 (1999).
[31] G. Lucovsky, R. J. Sladek, and J. W. Allen, Phys. Rev. B **16**, 4716 (1977).
[32] S. Foner, Phys. Rev. **130**, 183 (1963).
[33] A. H. Hill, A. Harrison, C. Dickinson, W. Zhou, and W. Kockelmann, Microporous Mesoporous Mater. **130**, 280 (2010).
[34] S.-W. Cheong and M. Mostovoy, Nature Mater. **6**, 13 (2007).
[35] A. Pimenov, A. M. Shuvaev, A. A. Mukhin, and A. Loidl, J. Phys.: Condens. Matter **20**, 434209 (2008).